ACS APPLIED MATERIALS & INTERFACES

www.acsami.org

Research Article

Enhanced Decomposition of Ammonium Perchlorate–Ethyl Cellulose–Molybdenum Disulfide Nanocomposites

Alfred J. Baca,*,⊥ Michael D. Garrison,⊥ Lidia Kuo, Feiyu Xu, Lawrence C. Baldwin, Alexander S. Hyla, Michael R. Zachariah, and Mark C. Hersam

Cite This: *ACS Appl. Mater. Interfaces* 2023, 15, 26799–26811

Read Online

ACCESS | Metrics & More | Article Recommendations | Supporting Information

ABSTRACT: Ammonium perchlorate (AP) is commonly used in propulsion technology. Recent studies have demonstrated that two-dimensional (2D) nanomaterials such as graphene (Gr) and hexagonal boron nitride (hBN) dispersed with nitrocellulose (NC) can conformally coat the surface of AP particles and enhance the reactivity of AP. In this work, the effectiveness of ethyl cellulose (EC) as an alternative to NC was studied. Using a similar encapsulation procedure as in recent work, Gr and hBN dispersed with EC were used to synthesize the composite materials Gr–EC–AP and hBN–EC–AP. Additionally, EC was used because the polymer can be used to disperse other 2D nanomaterials, specifically molybdenum disulfide (MoS_2), which has semiconducting properties. While Gr and hBN dispersed in EC had a minimal effect on the reactivity of AP, MoS_2 dispersed in EC significantly enhanced the decomposition behavior of AP compared to the control and other 2D nanomaterials, as evidenced by a pronounced low-temperature decomposition event (LTD) centered at 300 °C and then complete high-temperature decomposition (HTD) below 400 °C. Moreover, thermogravimetric analysis (TGA) showed a 5% mass loss temperature ($T_{d5\%}$) of 291 °C for the MoS_2-coated AP, which was 17 °C lower than the AP control. The kinetic parameters for the three encapsulated AP samples were calculated using the Kissinger equation and confirmed a lower activation energy pathway for the MoS_2 (86 kJ/mol) composite compared to pure AP (137 kJ/mol). This unique behavior of MoS_2 is likely due to enhanced oxidation–reduction of AP during the initial stages of the reaction via a transition metal-catalyzed pathway. Density functional theory (DFT) calculations showed that the interactions between AP and MoS_2 were stronger than AP on the Gr or hBN surfaces. Overall, this study complements previous work on NC-wrapped AP composites and demonstrates the unique roles of the disperagent and 2D nanomaterial in tuning the thermal decomposition of AP.

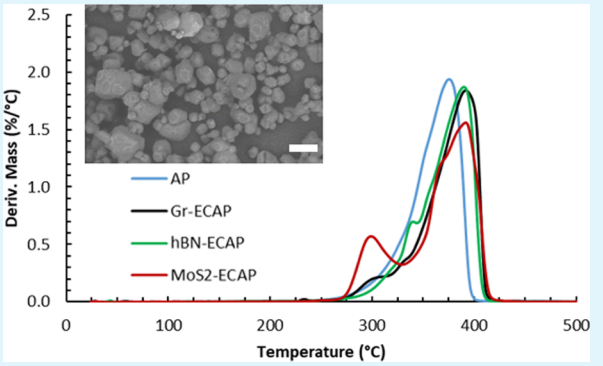

KEYWORDS: *graphene, hexagonal boron nitride, ethyl cellulose, molybdenum disulfide, ammonium perchlorate, morphology, crystallinity, 2D nanomaterials*

INTRODUCTION

Ammonium perchlorate (AP) is an oxidizer that is ubiquitous in the solid propulsion industry due to its high specific impulse (I_{sp}), reliable decomposition behavior, and excellent stability.[1−4] AP decomposition rates can be enhanced or reduced with chemical additives, which allows predictable control over burn rate for different propulsion applications.[4] In a typical solid propellant, AP comprises 60−90% of the formulation, so propellant behavior is highly dependent on AP properties.[4,5] Thus, a significant body of previous work has sought to establish a fundamental understanding of AP decomposition in an effort to guide improvements in propulsion technologies.[1−3] Despite these research efforts, no consensus has been reached on the AP decomposition mechanism because the reaction involves a complex interplay between solid state and chemical phenomena.

AP decomposition is typically studied from a solid-state chemistry perspective in which the reaction is initiated at defects in the solid lattice that serve as nucleation sites for decomposition.[1,7−9] AP crystals undergo a phase transition from orthorhombic to cubic at 240 °C, and the decomposition behavior of both polymorphs has been studied extensively in previous work.[6−8] However, the exact mechanism remains unclear due to the complexity of solid-state chemical reactions and the factors that affect such processes, including (1) particle size, (2) particle morphology, (3) reaction temperature

Received: March 20, 2023
Accepted: May 11, 2023
Published: May 23, 2023

(isothermal reactions), (4) heating rates (nonisothermal reactions), (5) pressure, (6) adsorption/desorption of product gases, and (7) the presence of chemical impurities or additives.[7,10] Thermal decomposition of AP is complex; for instance, pure AP typically shows two decomposition events during nonisothermal heating: (1) low-temperature decomposition (LTD) below 300 °C and (2) high-temperature decomposition (HTD) above 300 °C. After undergoing LTD, the resulting AP particles show morphological changes with the formation of porosity on the particle surface, which significantly increases the particle surface area, but without introducing chemical differences from pristine AP.[7,11−13] Decomposition typically ceases after LTD until the AP particles are heated to higher temperatures (>300 °C), and this inactivity between events has previously been attributed to the exhaustion of defects (nucleation sites) during LTD.[9,14] Consistent with this hypothesis, fine AP particles (<10 μm) typically do not show an LTD event because smaller crystals typically have lower defect levels and, thus, fewer nucleation sites than larger crystals.[8]

An alternate hypothesis for LTD cessation proposes that the adsorption of product gases (e.g., ammonia) onto the solid surface inhibits the decomposition reaction.[11,15,16] This hypothesis is supported by the differences in AP reactivity when studied in sealed containers where product gases cannot escape compared to open containers in which product gases can easily be removed. For example, AP typically shows two exothermic events representing LTD and HTD in a sealed container.[7,10] In contrast, AP decomposition in an open container or vacuum shows an exothermic LTD event and an endothermic HTD event, with the latter event representing the sublimation of AP.[7] Therefore, surface chemistry also plays a role in AP decomposition and can significantly alter the reaction mechanism. Overall, AP decomposition is a complex solid-state process where the exact mechanism depends on a variety of factors, such as defects and gas adsorption, which should be specified for meaningful comparison between studies.

Although most previous studies have focused on solid-state phenomena, AP decomposition should also be considered from a chemical perspective. The AP decomposition products have been studied by thermal analysis techniques coupled with mass spectrometry (MS) as well as Fourier transform infrared spectroscopy (FTIR), which show the formation of NH_3, H_2O, NO, O_2, HCl, N_2O, and NO_2 gases among other minor byproducts.[2,11,17] A proposed chemical mechanism for this decomposition process has been reported previously and is as follows[10,17]

$$NH_4ClO_4(s) \rightarrow NH_3(g) + HClO_4(g) \quad (1)$$

$$4HClO_4(g) \rightarrow Cl_2(g) + 5O_2(g) + 2ClO_2(g) + 2H_2O(g) \quad (2)$$

$$2Cl_2(g) + 2H_2O(g) \rightarrow 4HCl(g) + O_2(g) \quad (3)$$

$$2NH_3(g) + 2ClO_2(g) \rightarrow N_2O(g) + Cl_2(g) + 3H_2O(g) \quad (4)$$

$$N_2O(g) + O_2(g) \rightarrow NO(g) + NO_2(g) \quad (5)$$

Reaction 1 is a dissociative sublimation process that liberates NH_3 and $HClO_4$ gases and is facilitated by proton transfer between the ammonium cation and the perchlorate anion.[1,2] The HTD event is endothermic under low-pressure conditions and is typically affiliated with reaction 1.[7] Reaction 2 involves the decomposition of $HClO_4$ into oxidizing species such as ClO_2 and O_2, which can oxidize NH_3 to form N_2O, NO, and NO_2 as shown in reactions 4 and 5. Thus, two chemical pathways occurring in AP decomposition are proton transfer between the ammonium cation and the perchlorate anion to form the conjugate acid−base pair and oxidation−reduction (redox reaction) between NH_3 and $HClO_4$ decomposition products. In early studies, electron transfer between ammonium and perchlorate ions in the solid state was proposed to be critical to the decomposition pathway and help explain the formed decomposition products.[1,11] However, an electronic structure study showed that ammonium perchlorate is a dielectric with a large band gap (5.6 eV), which makes the electron transfer pathway unlikely in the solid state.[1,18] Alternatively, the electron transfer steps were determined to occur as secondary reactions in the gas phase or condensed phase on the solid surface after reaction 1 occurs.[1,19] LTD is an exothermic process under most reaction conditions and is hypothesized to be affiliated with these electron transfer pathways, likely on the AP crystal surface after sublimation and adsorption.[1,10] Because reaction 1 is a necessary step before reactions 2−4 can occur, both sublimation and redox reactions occur together during LTD, with the former process becoming dominant as AP decomposition reaches the HTD event.[7]

Recent studies have focused on improving the reactivity of AP via enhanced proton and electron transfer mechanisms. In particular, transition metals and metal oxides have been studied as AP burn rate enhancers, which likely catalyze AP decomposition via electron transfer pathways.[1,2] For instance, molybdenum disulfide (MoS_2) has been used as a decomposition catalyst for AP with improved safety due to the dry film lubricant properties of MoS_2.[20] Although metal compounds have a demonstrated catalytic effect, a new approach to AP decomposition catalysis involves the use of carbon-based materials such as polymeric carbon nitride, carbon nanotubes, graphene oxide (GO), and pristine graphene (Gr) as scaffolds to support transition metal catalysts.[21−28] These carbon materials exhibit high thermal stability and electrical conductivity, thereby enhancing electron transport between the metal catalyst and the AP substrate, and have demonstrated a synergistic effect when combined with metal catalysts, which is likely due to enhanced electron transfer.[27] For example, in a study on Mn_3O_4 nanoparticles combined with Gr, the Gr−Mn_3O_4 catalyst showed enhanced decomposition of AP but Gr alone showed negligible catalytic effects.[27] However, in more recent work, AP conformally coated with nitrocellulose (NC) and Gr demonstrated excellent catalytic properties for LTD without the use of a transition metal catalyst, which is likely due to the intimate contact between the materials that facilitated effective electron transfer.[28] In addition to promoting electron transfer, catalytic materials can be used to promote proton exchange for the sublimation reaction. This mechanism was observed in a study on AP combined with boron nitride (BN) materials, which showed no catalytic effects on their own but significantly lowered decomposition temperatures when modified with amines.[29] Despite these advances in AP catalysis, few studies have focused on the conformal coating of AP particles with "pristine" 2D nanomaterials, and the subsequent kinetic parameters and physical models.

https://doi.org/10.1021/acsami.3c04021
ACS Appl. Mater. Interfaces 2023, 15, 26799−26811

In an effort to address this knowledge gap, this work elucidates the kinetic and physical models for AP catalysis by investigating the decomposition behavior of AP after encapsulation with Gr, hexagonal boron nitride (hBN), and MoS_2 (2H-phase) using an ethyl cellulose (EC) dispersion and wrapping agent. Surprisingly, the use of EC as a dispersion agent showed a less pronounced LTD peak for Gr and a thermally stabilizing effect for HTD decomposition for 2D nanomaterial/EC coated AP, in contrast to previous work.[28] The encapsulated AP nanocomposites were studied using differential scanning calorimetry (DSC) and thermogravimetric analysis (TGA) to examine relative thermal stability. TGA coupled with mass spectrometry (MS) was also performed to examine the decomposition products and gain chemical mechanistic insight. Additionally, the systems of AP interacting with the 2D nanomaterials (Gr, hBN, and MoS_2) were studied computationally, using periodic density functional theory (DFT), to determine the most likely interaction configurations and gain insight into the differences in AP decomposition in the presence of these 2D nanomaterials. Finally, the solid-state reaction kinetics were studied using the Kissinger and Friedman models to calculate kinetic parameters as well as understand the physical models governing the decomposition processes of the modified materials. This work highlights the differences in AP decomposition with EC (dispersion agent) and different 2D nanomaterials (Gr, hBN, and MoS_2). Most prominently, AP showed significantly enhanced reactivity when combined with MoS_2 where the reaction appears to be limited by diffusion rather than nucleation, as has been observed in previous studies.

EXPERIMENTAL SECTION

Materials. Solvents were purchased from Fisher Scientific, and all reagents were used as received. Ammonium perchlorate (reagent grade) was purchased from Alfa Aesar. Gr−EC and hBN−EC powders were prepared as detailed in previous reports.[30,31] The Gr−EC and hBN−EC dispersions, prior to fabricating the AP nanocomposites, were prepared in a manner similar to previous work, replacing NC with EC.[28] MoS_2−EC powder was prepared by shear mixing the bulk MoS_2 powder (Sigma-Aldrich) with EC (Sigma-Aldrich, 4 cP) in ethanol. The dispersion was then centrifuged, flocculated with aqueous NaCl (4 vol %), vacuum filtered, and rinsed with deionized water. The MoS_2−EC powder contained 11 wt % MoS_2, as confirmed by TGA. The final MoS_2−EC dispersion used to fabricate the AP nanocomposites was prepared by bath sonicating a 10 mg/mL loading of the MoS_2/EC powder in ethanol. Details on characterization methods and kinetic calculations can be found in the Supporting Information (SI).

Fabrication of AP Nanocomposites. The synthesis of uncoated and coated AP crystals with 2D nanomaterials composed of Gr−EC, hBN−EC, and MoS_2−EC incorporates a process similar to the one demonstrated in recent work.[28] Briefly, 500 mg of neat AP solid was dissolved in 10 mL of methanol, and then a few drops of nanomaterials/EC solution was added to the mixture. The resulting solution was bath sonicated until the AP was completely dissolved. Once dissolved, the dispersion was added dropwise to a fast-stirring solution of chloroform, leading to the precipitation of AP nanocomposites. The bulk solvent was removed via decantation, and then the particles were dried in a vacuum desiccator overnight to remove the residual remaining solvent.

Calculation Methodology. To describe the graphene, hBN, and MoS_2 surfaces, a repeated-slab approach was used. The unit cells of graphene,[32] hBN,[33] and MoS_2[34] were made into 7 × 7, 4 × 4, and 4 × 4 supercells, respectively, and rotated from hexagonal to orthorhombic cells. The supercells were then allowed to fully relax the positions of the atoms, and the cell parameters were allowed to relax as long as the system stayed in the orthorhombic phase. Each slab of graphene and hBN consisted of a single layer of atoms of either only carbon for the graphene surface or an alternating pattern of boron and nitrogen for the hBN surface. The slab of MoS_2 had three layers, with a Mo layer in the middle and two S layers above and below. The slabs of atoms were separated by a vacuum layer larger than 20 Å along the *c*-axis to prevent interactions from period images in that direction. The lateral dimensions for the graphene supercell were 14.80 × 17.10 × 35.02 $Å^3$, while the lateral dimensions of the hBN surface were 10.04 × 8.70 × 35.00 $Å^3$. The lateral dimensions of the MoS_2 surface were 12.61 × 10.96 × 35.00 $Å^3$. We note here that the lattice parameters for graphene and hBN optimized at the DFT level with the PBE-D3BJ functional are very close to the experimental values, within 0.6 and 0.5%, respectively.[32,33] MoS_2 was slightly farther from experimental lattice parameters, at around 0.2% along the *a*-direction and 3% along the *b*-direction, and the slab did not initially want to optimize with vacuum space between the periodic images in the *c*-direction.[34]

All surface calculations were completed using the Quantum ESPRESSO program, version 7.1.[35,36] The calculations were performed with plane-wave basis sets with an energy cutoff of 50 Ry (~680 eV); the projector augmented wave (PAW) method[37] was used to describe the valence−core electron interactions. The generalized gradient approximation (GGA) exchange−correlation functional of Perdew, Burke, and Ernzerhof (PBE),[38,39] augmented by the empirical D3 dispersion correction of Grimme et al. with the Becke−Johnson damping,[40] was adopted in order to describe the nonspecific interactions occurring between the AP and the 2D nanomaterials. In order to examine the extent of charge transfer in these NHC systems, Bader charges were evaluated[41] (while it is difficult to assess the accuracy of atomic partial charges, these charges have an estimated error of less than 15%).[42] A 2 × 2 × 1 Monkhorst−Pack *k*-point grid was used for geometry optimizations for the unit cells both with and without AP, while a 12 × 12 × 1 Monkhorst−Pack *k*-point grid was used for self-consistent total-energy calculations. The Gaussian[43] occupation scheme with a smearing of 0.01 Ry (0.14 eV) was used for Brillouin zone integrations in the calculations.

Geometry optimizations were performed using the Broyden−Fletcher−Goldfarb−Shanno (BFGS) quasi-Newton algorithm[44] until the forces were <0.0001 au (8.24×10^{-12} N) for calculations on each of the surfaces. To compensate for possible dipole−dipole interactions between the asymmetric slabs, a dipole sheet was inserted into the vacuum gap.

Gas phase calculations of AP were performed using the Gaussian 16 program suite.[45] The AP geometry was optimized, and frequencies were calculated at the B3LYP-D3BJ/aug-cc-pVTZ level to ensure that a stationary point was found. The optimized geometry was then used in the periodic DFT calculations, placed above the 2D nanomaterials to create the different configurations examined.

The AP molecule was chosen to have 8 different orientations which could interact with the 2D nanomaterials, each with different numbers and types of atoms that could initially interact. These orientations are denoted 1H down, 2H down, 3H down, 1O down, 2O down, 3O down, 1H 1O down, and 2H 2O down. These configurations can be seen in Figure S1. The different orientations of AP were then placed in different locations on the 2D nanomaterial surface. The combination of an orientation of AP and a location in the unit cell will be called a configuration. The AP was started 3 Å above the topmost atom of the surface before geometry optimization. On the hBN surface, four different locations were chosen, assuming that each location was symmetry equivalent throughout the supercell (Figure S2). Those locations are directly above a boron atom, directly above a nitrogen atom, directly above the mid-point of a B−N bond, and directly above the center of a 6-membered ring containing both B and N, denoted above B, above N, mid B−N bond, and ring center, respectively. On the graphene surface, four different locations were also used. These locations are similar to the hBN locations but are denoted above the top right C, above the bottom right C, mid C−C bond, and ring center. The two different carbon positions were deemed symmetry inequivalent when the AP was added to the

https://doi.org/10.1021/acsami.3c04021
ACS Appl. Mater. Interfaces 2023, 15, 26799−26811

surface, potentially leading to interactions with different electronic environments (directly near a carbon atom or above the center of a 6-membered carbon ring). On the MoS_2 surface, five different locations were used. Four of these locations were similar to the hBN and graphene surfaces, denoted above Mo, above S, mid Mo−S bond, and ring center, but the multilayered structure of MoS_2 suggested that there may be another location in the middle of four S atoms that may have some influence on the interaction of AP with MoS_2, which is denoted above S diamond center.

RESULTS AND DISCUSSION

Differential scanning calorimetry (DSC) was performed on the AP control, Gr−EC−AP, hBN−EC−AP, and MoS_2−EC−AP to determine the thermal transitions (Figure 1). All materials

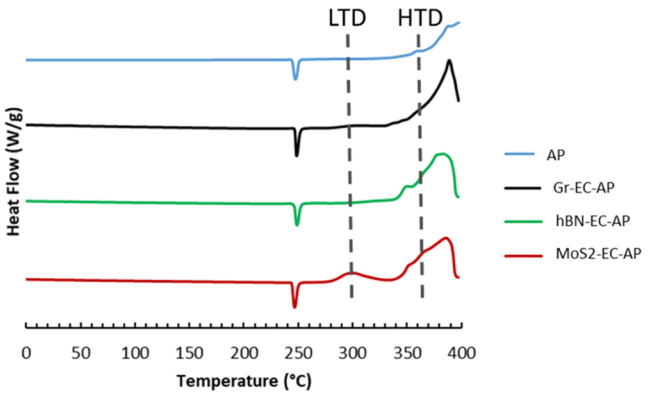

Figure 1. DSC results for AP and conformally coated AP samples (curves are offset in the y-axis for clarity). Analysis was performed on AP samples in sealed, hermetic pans with a pinhole at 10 °C/min. The LTD dashed line represents the upper limit temperature of LTD thermal events, and the HTD dashed line represents the onset of HTD decomposition for the uncoated AP.

showed an endothermic transition peaking between 247 and 249 °C, which represents the phase transition from the orthorhombic to cubic structure. This event had a consistent endotherm enthalpy (ΔH_{endo}) for all AP composites ranging from 100 to 112 J/g and was comparable to the value reported previously with nitrocellulose-wrapped AP (94−99 J/g).[28] Thus, the result implies that the EC or the wrapping agent (i.e., 2D nanomaterial) does not affect the crystalline structure or phase transitions of AP. A detailed analysis of the powder XRD (PXRD) (Figure S3) reveals subtle crystallinity differences not shown in the DSC data. The peak heights/intensities of the indexed reflections [101], [200], and [210] change, which may indicate crystal habit modification.[46] Scanning electron microscopy (SEM) images show that the particle sizes varied depending on the 2D nanomaterial. This implies that the judicious choice of 2D nanomaterial disperagent could have an effect on the morphology of the AP nanocomposites (Figures S4−S6).

Following the orthorhombic to cubic phase transition, the exothermic decomposition of AP was observed. An LTD peak for the AP control was not observed in this study, likely due to small particle size (<20 μm), thus leading to a fewer number of defects available to initiate AP LTD.[8] The AP control began to decompose at 340 °C but did not fully react below 400 °C, which was the upper-temperature limit for the DSC instrument. In comparison, the 2D-AP nanocomposites showed more complete exothermic events. Gr−EC−AP had a small, broad peak centered at 300 °C representing LTD, but the peak was much smaller than the LTD peak observed in previous studies with NC used as the wrapping agent.[28] This result implies that the nanomaterial formed from EC and Gr does not have a strong catalytic effect on AP decomposition like that of NC and Gr.[28] In previous work by Secor et al., printed graphene with NC showed enhanced conductivity compared to EC, which is likely the reason for the differences in reactivity for Gr−EC−AP compared to Gr−NC−AP.[47] The hBN−EC−AP composite did not show an LTD event but did show a low-temperature shoulder that could represent an enhanced HTD event, which is similar to the decomposition behavior of the NC analogue in previous work.[28] Interestingly, MoS_2−EC−AP showed a significant LTD event centered at 300 °C (Figure S7), then complete HTD below 400 °C. Thus, MoS_2 enhanced the decomposition behavior of AP compared to the control and other 2D nanomaterials.

The enhanced reactivity of AP mixed with MoS_2 has been demonstrated in previous work in which MoS_2−AP powders were prepared from the 2H-MoS_2 (semiconducting) and 1T-MoS_2 (metallic) phases.[20] In that previous work, AP had significantly enhanced decomposition when combined with 1T-MoS_2 but only at high loading (20 wt %).[20] At low loadings of 1T-MoS_2 (1 wt %), the previously reported 1T-MoS_2−AP composite demonstrated decomposition behavior similar to that of the MoS_2−EC−AP composite in this study, which involves the 2H-phase (Figure S8).[20] This comparison implies that the conductivity of MoS_2 is likely not the most significant factor in catalytic activity. Furthermore, considering that graphene is an electrical conductor and hBN is an insulator, the 2H-MoS_2−EC−AP composite would be expected to have intermediate reactivity compared to the other 2D nanomaterials if conductivity was the dominant factor, but the improved reactivity of MoS_2−EC−AP indicates that other properties play a larger role in enhanced AP decomposition. One potential hypothesis for the enhanced MoS_2 reactivity is that the 2D nanomaterial decomposes to provide a transition metal catalyst (MoO_x species) for enhanced electron transfer reactions. MoO_3 has previously demonstrated a catalytic effect on AP decomposition and is typically formed from the oxidation of MoS_2.[48,49] Thus, the formation of catalytic MoO_3 was hypothesized to occur during the early stages of MoS_2−EC−AP decomposition with the initial products ($HClO_4$, O_2, ClO_2, and Cl_2) accelerating the oxidation of the MoS_2 nanomaterial. To check this hypothesis, TGA was performed on both EC−MoS_2 and EC in nitrogen and air to determine the thermal and thermo-oxidative stability (Figures S9 and S10). EC and MoS_2−EC both decomposed at a low temperature in air (<300 °C), and MoS_2−EC showed additional mass loss above 400 °C, which likely represents oxidation of MoS_2. Therefore, this TGA experiment in air does not support the hypothesis that MoS_2 is oxidized to MoO_3 as the active catalyst for MoS_2−EC−AP decomposition, but the possibility cannot be completely ruled out because other decomposition products (such as $HClO_4$ and ClO_2) have greater oxidizing power than O_2. Another potential hypothesis could be an increased number of sulfur vacancies on the MoS_2 that provide catalytic sites at defects in the 2D nanomaterial, which have previously been exploited for other reactions, such as hydrogen synthesis.[50] Solution-processed 2D materials, as used in this case, are known to produce a larger concentration of defects.[51] X-ray photoelectron spectroscopy (XPS) on MoS_2−EC showed a stronger oxysulfide-related peak compared to the S2p peak, which indicates a high sulfur vacancy

https://doi.org/10.1021/acsami.3c04021
ACS Appl. Mater. Interfaces 2023, 15, 26799−26811

content (Figure S11). As a result, these MoS_2 defect sites may also play a role in the enhanced decomposition of MoS_2–EC–AP if the MoS_2 does not oxidize during the initial stages of the reaction.

Thermogravimetric analysis (TGA) was also performed on the AP materials (Figure 2). TGA showed slightly different

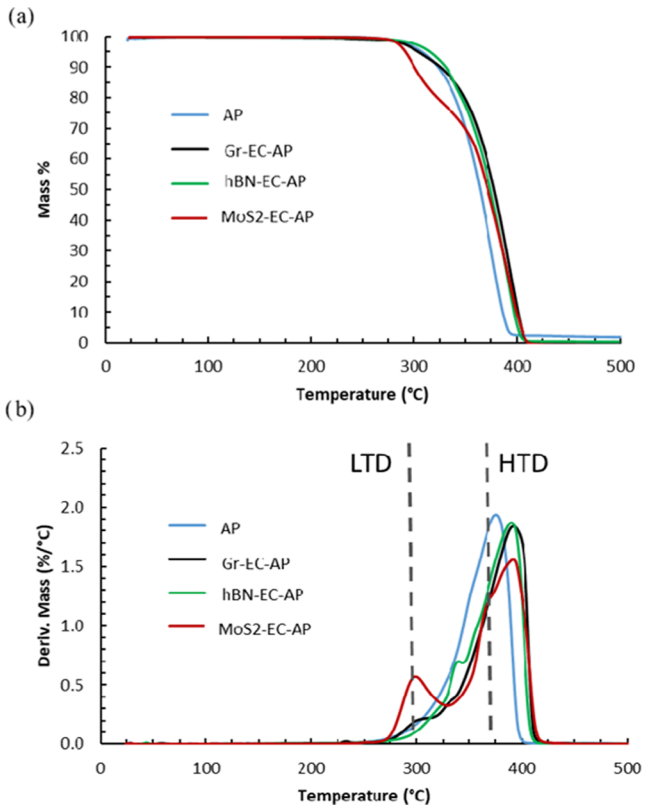

Figure 2. TGA results for AP and conformally coated AP samples (Heating Rate: 10 °C/min) showing (a) mass loss and (b) derivative mass loss versus temperature.

decomposition behavior due to the different sample containers and flow rates used for TGA analysis, which results in different pressure and heat distributions that can affect decomposition behavior.[7] Unexpectedly, the Gr–EC–AP and hBN–EC–AP had slightly higher decomposition temperatures than the AP control under these conditions. At a heating rate of 10 °C/min, the temperature at 5% mass loss ($T_{d5\%}$) for Gr–EC–AP and hBN–EC–AP were 304 °C and 315 °C, respectively, compared to 308 °C for the AP control. In contrast, the MoS_2–EC–AP had the lowest $T_{d5\%}$ at 291 °C. The temperature at 10% mass loss ($T_{d10\%}$) further showed these differences in reactivity. The AP control had a $T_{d10\%}$ of 323 °C, whereas Gr–EC–AP and hBN–EC–AP had slightly higher values at 325 and 330 °C, respectively. Mirroring the $T_{d5\%}$ trends, MoS_2–EC–AP had a significantly lower $T_{d10\%}$ at 300 °C, which was 23 °C lower than the control and highlighted the catalytic behavior of MoS_2. The LTD event for MoS_2–EC–AP involved a 20% decrease in mass before the inflection point, which was more pronounced than the LTD event observed for Gr–NC–AP in previous work.[28]

The TGA derivative curves provide additional clarity and further highlight the differences in reactivity between the control and coated AP composites. MoS_2–EC–AP showed an LTD event peaking at 304 °C and a larger HTD peak at 385 °C. These two events were consistent with the DSC results for MoS_2–EC–AP. Gr–EC–AP had a less pronounced LTD peak than MoS_2–EC–AP at 300 °C that merged with the HTD peak. The small LTD peak for Gr–EC–AP further demonstrates that EC–Gr has a less significant effect on AP decomposition than MoS_2 and NC–Gr as reported previously.[28] The HTD event for Gr–EC–AP peaked at 392 °C, which was 16 °C higher than the AP control peak decomposition temperature at a 10 °C/min heating rate. Additionally, hBN–EC–AP had a shoulder peaking at 336 °C that merged with the main decomposition event that peaked at 389 °C, which is consistent with the DSC results. Overall, MoS_2–EC–AP had a significant LTD peak, but the HTD peaks of all 2D nanomaterial composites were shifted to higher temperatures than the AP control. The use of EC as a 2D nanomaterial dispersion agent thermally stabilizes the AP as will be described in the kinetics section of this paper.

To further study thermal stability, the AP composites were also analyzed via simultaneous DSC/TGA (SDT) thermal analysis, which allowed for higher temperature DSC analysis (>400 °C) and showed the heat flow of decomposition in an open pan environment (Figure 3). The TGA curves were

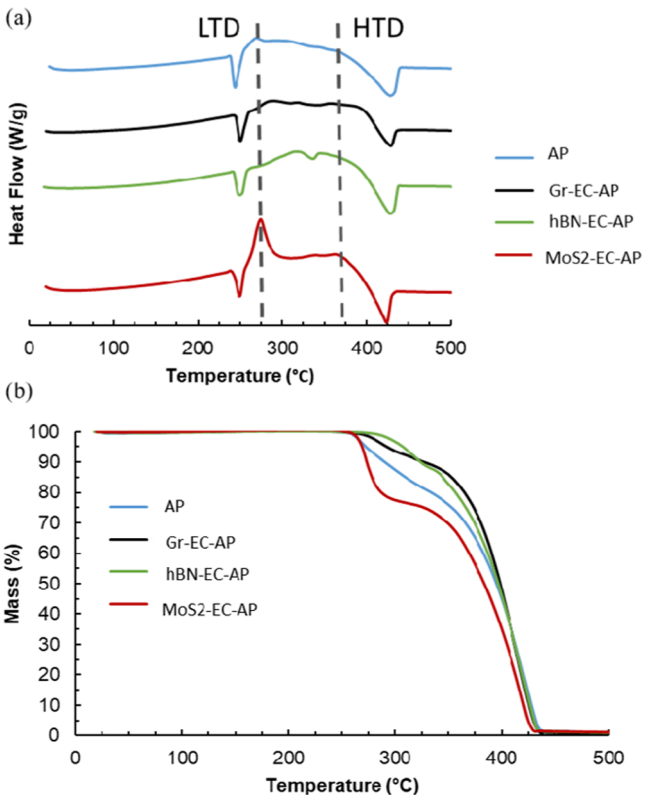

Figure 3. Thermal results from the simultaneous DSC/TGA (SDT) analysis showing (a) heat flow (DSC) and (b) mass loss (TGA) of decomposition. Samples were analyzed at 5 °C/min in an open crucible under argon gas. DSC curves were y-offset for comparison.

consistent with the results in Figure 2, as expected, but the DSC curves generally showed less pronounced, broader exotherms than Figure 1. This behavior is typical for AP decomposition in open pans because the competing sublimation mechanism becomes more favorable compared to closed-pan environments due to the facile removal of product gases.[7,10] All AP materials had an endothermic peak at 425 °C

https://doi.org/10.1021/acsami.3c04021
ACS Appl. Mater. Interfaces 2023, 15, 26799–26811

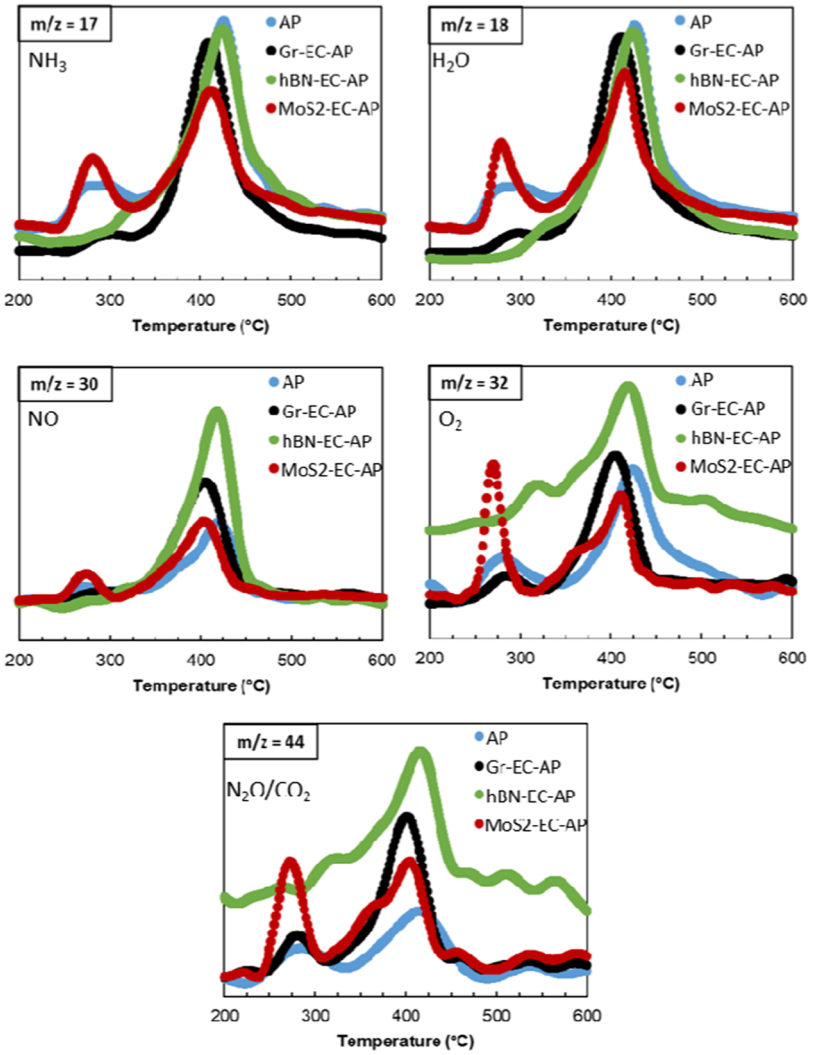

Figure 4. GC-MS results from the decomposition gases of the AP composite materials.

that represents sublimation at the end of the decomposition reaction and has been reported in previous studies.[7,27] MoS_2−EC−AP showed decomposition behavior similar to AP, Gr−EC−AP, and hBN−EC−AP at temperatures >300 °C, but a sharp exothermic peak was observed at 275 °C, representing the LTD event. This peak further highlights the catalytic effect of MoS_2 in promoting AP decomposition and suggests that the catalytic effect is likely due to an oxidation−reduction mechanism rather than dissociative sublimation, which would show a larger endotherm considering AP sublimation is an endothermic process.

The decomposition gases were analyzed via GC-MS during SDT thermal analysis to obtain additional insight into the decomposition mechanism of the AP composites (Figure 4). NH_3, H_2O, NO, O_2, HCl, N_2O, and NO_2 are known byproducts of AP decomposition, so mass-to-charge ratios (m/z) of 17, 18, 30, 32, 36, 44, and 46, representing the maximum m/z ratios for each ionized species, respectively, were studied. CO and CO_2 (peak m/z values at 28 and 44, respectively) are other possible byproducts resulting from EC decomposition and were considered. However, no peak was observed for CO, indicating that the EC amount is likely too low for the detection or the EC is fully oxidized to CO_2 and could not be differentiated from N_2O. The HCl (Figure S12) and NO_2 signals were weak for all AP materials. For HCl, this signal was likely low due to the reaction of the strong acid with the transfer line prior to MS analysis.[28] The absence of a NO_2 peak implies that the N_2O does not fully oxidize under these reaction conditions.

Compared to the composites with 2D nanomaterials, the GC-MS results for pure AP showed divergent decomposition product gas distributions. For the AP control, small amounts of NH_3, H_2O, NO, O_2, and N_2O/CO_2 were observed at 300 °C during LTD. Because NH_3 and NO were observed simultaneously, the m/z = 44 peak most likely represents N_2O, which is a product of NH_3 oxidation rather than CO_2. During HTD of the AP control at 400 °C, significant amounts of all five decomposition products were observed. Considering that the SDT DSC results show an endotherm during HTD, sublimation is the dominant mechanism during this reaction, but the presence of NH_3 as well as oxidized NH_3 products (NO, N_2O) also implies that a mixed mechanism with oxidation−reduction is occurring simultaneously. As was observed in previous work, oxidation−reduction reactions between the perchloric acid decomposition products and NH_3 can occur in the gas phase after sublimation, which explains why these products are also observed when sublimation is the predominant mechanism during HTD.[1,19] Thus, as a baseline

https://doi.org/10.1021/acsami.3c04021
ACS Appl. Mater. Interfaces 2023, 15, 26799−26811

Table 1. Kinetic Parameters for AP Decomposition Calculated Using the Kissinger Model

2D material	wrapping agent	E_a (kJ/mol)	A (s^{-1})	R^2	reference
none	none	137 (HTD)	3.69×10^7	0.9897	28
Gr	NC	145 (LTD)	1.77×10^{10}	0.9783	29
		121 (HTD)	2.03×10^6	0.9933	
Gr	EC	153 (HTD)	3.65×10^8	0.9657	this work
hBN	NC	129 (HTD)	9.23×10^6	0.9501	28
hBN	EC	132 (HTD)	5.11×10^6	0.9850	this work
2H-MoS_2	EC	86 (LTD)	1.90×10^4	0.9854	this work
		190 (HTD)	7.63×10^{11}	0.9677	
2H-MoS_2	none	178 (HTD)	1.11×10^{10}[a]	0.9671	20
1T-MoS_2	none	120 (HTD)	5.68×10^5[a]	0.9940	20

[a]Values were calculated from the previous study using reported data and the Kissinger equation.

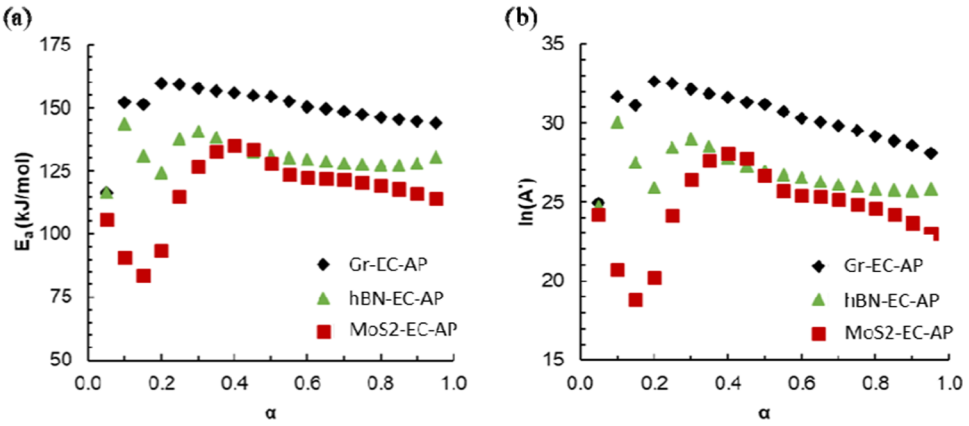

Figure 5. Plots of kinetic parameters calculated from the TGA results and Friedman Model for the AP materials. The relationship between the degree of conversion (α) and activation energy (Ea) is shown in (a), whereas α versus the natural logarithm of the modified Arrhenius factor [$A' = f(\alpha)*A$] is shown in (b).

for comparison, the decomposition of the AP control showed a mixed mechanism with sublimation and formation of oxidation−reduction products in the gas phase. The same decomposition behavior was observed for Gr−EC−AP and hBN−EC−AP, except that the LTD events were less pronounced for these materials, which was expected and consistent with the DSC, TGA, and SDT results. In contrast, MoS_2−EC−AP showed significant amounts of all five decomposition products at 275 °C during LTD. The LTD peak heights for NH_3, H_2O, and NO were roughly half the intensity of the respective HTD peak heights during MoS_2−EC−AP decomposition, and the O_2 and N_2O LTD peak heights were larger than the respective HTD heights. The exothermic event in the SDT DSC results, as well as the relatively large O_2 peak at 275 °C, imply that MoS_2 promotes reduction of $HClO_4$, which releases significant amounts of O_2 gas upon decomposition (eq 2). Also, exothermic events are typically affiliated with oxidation−reduction of AP (typically in high-pressure, sealed container analyses), so oxidation−reduction is likely the predominant mechanism occurring during LTD of MoS_2−EC−AP, with sublimation playing a minor role.[1,10] Additionally, the relatively large N_2O peak shows an increased rate of partial NH_3 oxidation during LTD, which is likely due to higher concentrations of NH_3 and O_2 gases after the reduction of $HClO_4$.

The TGA results at different heating rates (1, 5, 10, 15, and 20 °C/min) were analyzed using the Kissinger model to determine the activation energy (E_a) and Arrhenius factor (A). The model was applied to LTD and HTD events for the AP composites when the two events showed distinguishable peaks in the TGA derivative curves at all five heating rates. The calculated values for this study are summarized in Table 1, which also includes relevant results from previous studies for comparison. Gr−EC−AP had an E_a value of 153 kJ/mol for the HTD decomposition event, which was larger than the AP control (E_a = 137 kJ/mol) and Gr−NC−AP (E_a = 121 kJ/mol) in the previous study.[28] Thus, EC−Gr appears to promote greater thermal stability in AP despite the presence of graphene and unlike NC−Gr. In contrast, hBN−EC−AP had an E_a of 132 kJ/mol, which was similar to hBN−NC−AP (E_a = 129 kJ/mol) in the previous study.[28] The E_a values for hBN-coated AP confirm that hBN does not have a significant catalytic effect on AP decomposition because hBN is an electrical insulator and does not impact oxidation−reduction. This finding was also observed in a previous study by Grossman et al. on amine-modified BN−AP composites, which showed no catalytic effect by multiple forms of BN except when combined with primary amines.[29] However, the high thermal conductivity of hBN can promote better heat transfer to AP, which likely contributes to the slightly lower calculated E_a values of the hBN−AP materials compared to the control. More notably, MoS_2−EC−AP had an E_a value of only 86 kJ/mol for LTD, which further demonstrates the catalytic effect of MoS_2 on AP decomposition. For the HTD event, MoS_2−EC−AP had a significantly higher E_a value at 190 kJ/mol, which is comparable to the 178 kJ/mol observed with 2H-MoS_2 (no wrapping agent) in a previous study.[20] MoS_2−EC−AP also possesses a significantly higher A value compared to

https://doi.org/10.1021/acsami.3c04021
ACS Appl. Mater. Interfaces 2023, 15, 26799−26811

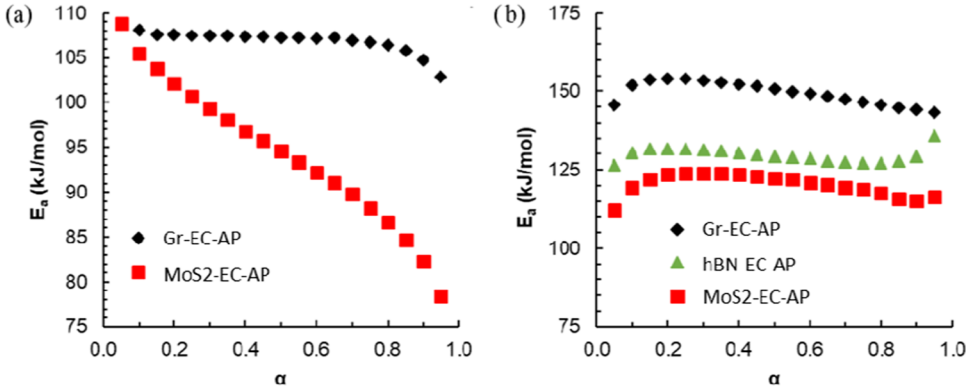

Figure 6. Relationships between E_a and α for the deconvolved (a) LTD and (b) HTD events for Gr−EC−AP, hBN−EC−AP, and MoS_2−EC−AP.

the other AP materials at 7.63×10^{11} s^{-1}, which demonstrates a larger number of successful collisions and enhanced reaction rate. The observed kinetic behavior for MoS_2−EC−AP is typical for transition metal-catalyzed AP decomposition. For example, a GO-triaminoguanidine nickel complex also showed relatively low E_a and A values during AP LTD of 120 kJ/mol and 8.91×10^4, respectively, but much higher values were observed during the HTD event (E_a = 181 kJ/mol and A = 2.34×10^9).[25] This reaction behavior was also observed for AP decomposition using a carbon nitride−CuO catalyst.[21] Thus, MoS_2 likely has a catalytic mechanism similar to other transition metal complexes based on the comparable kinetic behavior with other studies, which typically involves enhanced oxidation−reduction.

Additionally, the decomposition kinetics of the AP materials were analyzed using the Friedman model, which is a derivative isoconversional model that allows kinetic parameters to be calculated at different degrees of conversion (α).[52,53] Although the Kissinger method is useful for kinetic calculations and is commonly reported in the literature, the method is limited because the equation only calculates the parameters at one α value (the peak decomposition temperature). Also, the Kissinger model assumes a first-order reaction mechanism, which may not fully represent the actual solid-state mechanism. Therefore, isoconversional models were also explored to gain more insight into the entire decomposition reaction and potentially determine the solid-state reaction mechanism.

The kinetic parameters calculated from the Friedman method are shown in Figure 5, and slight differences in reactivity were observed for the various AP nanocomposites during HTD when compared to the Kissinger model results. The Friedman plots from the TGA results had linear fits for each AP material at each α value with $R^2 > 0.97$, except for MoS_2−EC−AP at α between 0.80 and 0.95, which had $R^2 > 0.93$ (Tables S2−S4 and Figures S13−S14). Gr−EC−AP had the highest E_a values for the decomposition reaction. At α = 0.05, Gr−EC−AP had a low E_a of 116 kJ/mol, likely representing the small LTD shoulder observed in the derivative TGA and DSC curves. However, for the remainder of the reaction, Gr−EC−AP had E_a values between 144 and 160 kJ/mol, which was higher than the values reported previously for the AP control.[28] The kinetic parameters for hBN−EC−AP were inconsistent for α values between 0.05 and 0.20 with an initial value of 116 kJ/mol that peaked to 141 kJ/mol (α = 0.10) and then decreased to 124 kJ/mol at α = 0.20. The erratic kinetic values imply a complex LTD mechanism likely representing multiple reactions occurring simultaneously, considering the reported values from isoconversional models represent a composite value for all reactions at a given α. This result would be expected because the low-temperature peak for hBN−EC−AP completely overlaps with the HTD peak at ∼330 °C at a 10 °C/min heating rate (Figure 2). At $\alpha \geq 0.25$, the kinetic parameters for hBN−EC−AP become more consistent and had E_a values between 127 and 141 kJ/mol. In comparison, MoS_2−EC−AP had the lowest E_a values over the course of the reaction for all AP materials. For α between 0.05 and 0.25, the E_a values ranged from 83 to 115 kJ/mol. The initial E_a value was 106 kJ/mol and decreased to a minimum of 83 kJ/mol at α = 0.15. For $\alpha > 0.25$, the E_a values (114−135 kJ/mol) were consistently higher than the initial stages of decomposition but still lower than the other AP materials. Thus, even though the DSC and TGA results only showed enhanced LTD, the Friedman model suggests that MoS_2 has a catalytic effect on AP decomposition by promoting low-energy decomposition pathways throughout the entire decomposition reaction (LTD and HTD). This hypothesis was also confirmed after analyzing the data with the Flynn−Wall−Ozawa (FWO) method, which is an integrative isoconversional method (these additional results are summarized in Tables S2−S4). Finally, natural-log-scale A values were also plotted in Figure 5, which showed the same trends as the E_a values for each AP material, likely due to the kinetic compensation effect, which describes the linear relationship between E_a and A for similar reactions.[54,55]

Due to the significant differences in kinetic parameters during the initial stages of the decomposition reactions, the peaks from the TGA derivative curves were deconvoluted using the Fraser−Suzuki method to gain more insight into the decomposition reaction at different stages. After deconvolution, the Friedman model was applied to the resulting curves to determine the kinetic parameters, and the E_a values are shown in Figure 6 for the LTD and HTD events. Gr−EC−AP had consistent LTD E_a values between 107 and 109 kJ/mol up to α = 0.75 but then showed a slight but steady decrease to 103 kJ/mol by α = 0.95 (Figure 6a). In the previous study on Gr−NC−AP, the LTD event did not show consistent E_a values over the course of the reaction and had a high initial E_a of 141 kJ/mol that gradually decreased to 72 kJ/mol, which was attributed to an electron transfer mechanism from pristine Gr to initiate LTD.[28] In the same study, NC−AP had steady but significantly lower E_a values during decomposition between 79 and 89 kJ/mol due to catalysis from nitrocellulose.[28] Thus, considering the Gr−EC−AP LTD decomposition behavior is more similar to NC−AP than Gr−NC−AP, the small catalytic

https://doi.org/10.1021/acsami.3c04021
ACS Appl. Mater. Interfaces 2023, 15, 26799−26811

effect observed for Gr−EC−AP LTD may involve a similar proton transfer mechanism from ethyl cellulose, which was observed with nitrocellulose only, with negligible enhancements from Gr. This difference in reactivity for Gr−EC versus Gr−NC is likely due to the differences in conductivity between the two materials, which was observed in a previous study.[47] In contrast to Gr−EC−AP, MoS_2−EC−AP had a comparable initial E_a value of 109 kJ/mol at α = 0.05, which more drastically decreased to 78 kJ/mol. For MoS_2−EC−AP, the kinetic behavior was like that of Gr−NC−AP in the previous study and suggests that electron transfer is a more likely pathway than a proton transfer kinetic mechanism.[28] The HTD events for all three coated AP materials showed consistent E_a values after deconvolution, and the kinetic parameters showed the same trends, with Gr−EC−AP having the highest E_a values and MoS_2−EC−AP having the lowest (Figure 6b).

Finally, the physical mechanisms for the AP composite LTD and HTD events were explored after the deconvolution of the derivative peaks (Figure 7). This process was performed in a

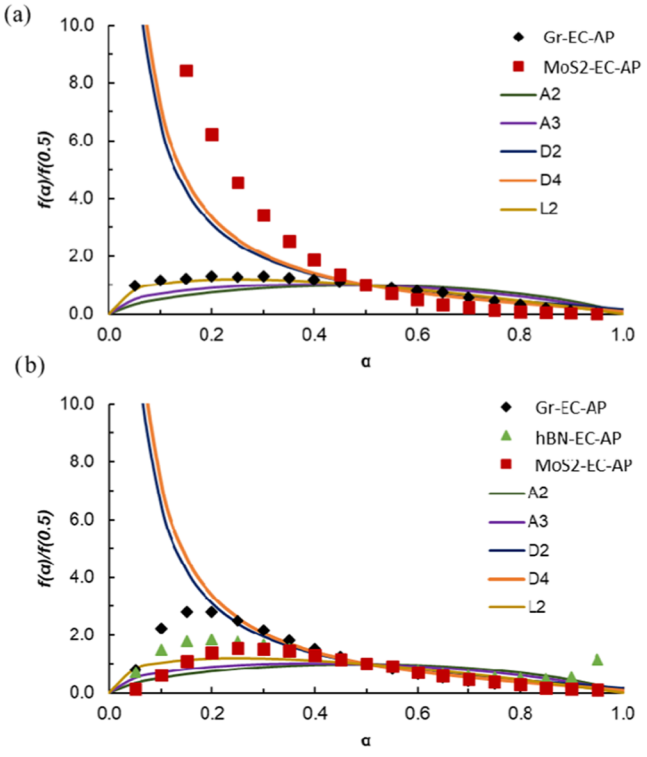

Figure 7. Normalized kinetic curves for the AP materials compared to common kinetic models for the (a) LTD and (b) HTD events. The kinetic models used as a baseline for comparison were the two-dimensional and three-dimensional growth of nuclei models (A2 and A3), the diffusion models (D2 and D4), and the random scission model (L2).

previous study in which the A' values [$A' = A^*f(\alpha)$] were normalized with the A' value at α = 0.50, and the resulting values [$f(\alpha)/f(0.5)$] can be compared to the normalized values for the physical kinetic models.[25] This technique assumes a constant A factor over the course of the reaction, which may be an oversimplification due to multiple reaction mechanisms occurring simultaneously, but it still provides deeper insight into physical reaction phenomena.[25] For the LTD results, Gr−EC−AP showed a good fit with the random scission model (L2), which is typically applied to polymer decomposition.[55] Hypothetically, the L2 model may appropriately represent the decomposition of the polymeric EC wrapping agent. However, an LTD event was not observed for hBN−EC−AP, which also contained EC, and the SDT-MS results showed AP decomposition products (NH_3, H_2O, NO, N_2O) during the Gr−EC−AP LTD event in addition to the potential EC decomposition products (H_2O, CO_2, but no CO). Thus, although the normalized Gr−EC−AP LTD data closely fit the L2 model, the more accurate description would be random nucleation rather than random scission since experimental evidence shows that the solid AP decomposition products predominantly form, and the EC polymer decomposition products could not be distinguished separately. The MoS_2−EC−AP LTD event did not have a good fit with any of the typical models but was most similar to the diffusion models (D2 and D4), considering the $f(\alpha)/f(0.5)$ values were large at the initial stages of the reaction and then rapidly drop as the reaction progresses. In the previous work by An et al., the decomposition behavior of AP changed from a contracting area or volume model (R2 or R3) for the pure, unmodified material to a two-dimensional growth of nuclei model (A2) after the addition of transition metal catalysts, which implied the metal centers act as nucleation sites for decomposition.[25] In contrast, this work shows a diffusion-based model for the MoS_2 catalyzed LTD of AP, and this model fit implies that the reaction may be limited by diffusion of reactants between the interface of the two solid materials (AP and MoS_2) or removal of product gasses from the reaction interface.[56,57] Considering the AP particles are conformally coated with the MoS_2 2D nanomaterial, the former scenario is likely because the distance between the two solids is initially small but grows as the reaction progresses. Moreover, this study focused on TGA data for the kinetics of AP-coated crystals, which has a low-pressure environment that favors endothermic sublimation. In contrast, a previous study performed kinetics analysis on DSC results that were collected in a higher-pressure exothermic environment.[25] Thus, the low-pressure environment in this study likely promotes the diffusion mechanism observed in this study over the nucleation mechanism observed in previous work that focused on closed-pan experiments. As a result, the reaction rate of MoS_2−EC−AP slows significantly toward the later stages of LTD (α > 0.4) due to the larger distance between the AP and Mo-based catalyst as the reaction progresses.

For the HTD events, all three AP materials had similar curve shapes with the highest $f(\alpha)/f(0.5)$ values at α values between 0.15 and 0.30. The curve shapes for all three materials showed the closest resemblance to the A2, A3, and L2 models for α < 0.35, but the $f(\alpha)/f(0.5)$ values were typically much higher than for the standard model. For Gr−EC−AP, the initial value of $f(\alpha)/f(0.5)$ rapidly increased and peaked at α = 0.15, which did not correlate well with any of the standard models. At α > 0.20, the HTD behavior of Gr−EC−AP resembles the D2 model, which implies a diffusion-limited process under these reaction conditions. This behavior was also observed for the HTD events of hBN−EC−AP and MoS_2−EC−AP, which had lower maximum $f(\alpha)/f(0.5)$ values than Gr−EC−AP during the initial stages of the reaction but still followed the D2 model at $\alpha \geq 0.35$. However, hBN−EC−AP did show some deviation from the D2 model at $\alpha \geq 0.90$. Overall, the HTD behavior for all AP materials was similar to the contracting area/volume and nucleation models at lower α values but matched the diffusion models at higher α values, which implies two competing

https://doi.org/10.1021/acsami.3c04021
ACS Appl. Mater. Interfaces 2023, 15, 26799−26811

mechanisms occur simultaneously. Although the $f(\alpha)/f(0.5)$ values were much higher than the standard A2, A3, and L2 models at $\alpha > 0.5$, this discrepancy was likely due to competing oxidation−reduction and sublimation mechanisms during the initial stages of HTD. The SDT results also showed a mixed mechanism of sublimation and oxidation−reduction (with the latter potentially occurring as a secondary reaction in the gas phase as well) in which sublimation becomes predominant at the end of the reaction. Thus, the reaction behavior most likely matches the A2/A3 and L2 models initially when oxidation−reduction is dominant and limited by particle surface area/volume and nucleation. At higher α values, the diffusion models are more representative of HTD for all AP materials because sublimation becomes the dominant mechanism, and the removal of product gases becomes the limiting process with the open pan reaction conditions.

Calculation Results. Following the optimization of the AP molecule in different orientations above the unique locations in each 2D material supercell, the minimum energies were compared to determine which were accessible at room temperature. For AP above the hBN surface, 21 of the 32 configurations studied were within 25.1 meV of the ground state configuration. For reference, the thermal energy at room temperature (298.15 K) is 25.7 meV. For AP on Gr, 27 of the 32 configurations were within 23 meV of the ground state, minimum energy configuration. With AP above the MoS_2 surface, only 13 of the 40 configurations were accessible at room temperature, but 5 additional configurations were accessible within an additional 20 K of thermal energy. At the higher temperatures required for AP decomposition (300 °C for LTD and 400 °C for HTD), a larger number of the configurations of AP were found to be accessible on each 2D material. The AP above hBN had 1 additional configuration accessible at LTD, compared to room temperature, and no additional new configurations accessible at HTD, for a total of 22 configurations accessible at both LTD and HTD. AP on Gr had 3 additional configurations accessible at LTD and no additional new configurations accessible at HTD, for a total of 30 configurations accessible at both LTD and HTD. AP on MoS_2 had the largest increase in the number of configurations accessible at LTD, going from 13 at room temperature to 34 accessible configurations at LTD, and 1 additional configuration was accessible at HTD, for a total of 35 configurations accessible out of the 40 studied. Upon further inspection of the optimized positions of AP on the surfaces, the AP on hBN was found to optimize in a similar orientation, in a similar position within the unit cell, hence the similar energies of the overall interacting system. These large numbers of configurations that are thermally accessible at room temperature suggest that the interaction between the AP and the 2D nanomaterial is not very dependent on the initial configuration because the desired interactions between the AP and the surfaces are fairly specific, which is seen in catalytic interactions.

One way to confirm the strength of binding interactions is by comparing the interaction energies. The interaction energies are calculated by subtracting the energies of the isolated components from the energy of the entire interacting system, and a negative value of the interaction energy means that the combined interacting system is more energetically favored than the isolated components. The lowest energy configurations of AP on the hBN, Gr, and MoS_2 surfaces each had the largest interaction energies of the configurations studied. Figure 8 shows the most energetically favored

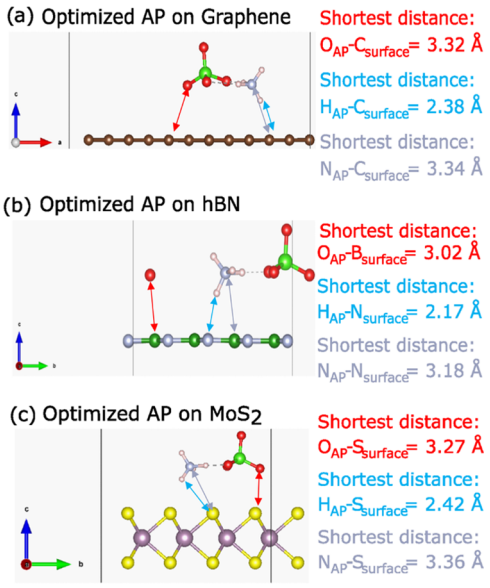

Figure 8. Minimum energy configurations of AP on the 2D nanomaterial surfaces (a) graphene, (b) hBN, and (c) MoS_2 as optimized by DFT (PBE-D3BJ/PW). The shortest distances between the different H, O, and N atom types in AP with the surface atoms are presented. The AP atoms were initially 3 Å above the top of the surfaces. Smaller distances indicate attractive interactions between the AP and the 2D nanomaterial.

configurations for AP on each 2D nanomaterial and the interatomic distances between the AP and the corresponding surface atoms. The interaction energy of the 1O down orientation of AP above the bottom right C configuration on Gr was −0.53 eV. The interaction energy of the 3H down orientation of AP above a ring center configuration on hBN was −0.68 eV. The interaction energy of the 1O down orientation of AP above a Mo atom configuration on the MoS_2 surface was −2.85 eV. This was a four- or five-time increase in the interaction energy for AP on the MoS_2 surface compared to the hBN and graphene surfaces.

Another confirmation of binding in these systems is to look at the interatomic distances between the AP and the 2D nanomaterial surface before and after geometry optimization. The AP atom(s) that were oriented closest to the surface were initially 3 Å above the topmost atom of the 2D nanomaterial surfaces. Figure 8 shows the most energetically favored configurations for AP on each 2D nanomaterial and the interatomic distances between the AP and the corresponding surface atoms. It should be noted that the distances presented in Figure 8 are not accounting for the thermal vibrations, rotations, and translations that are going to occur at the temperatures observed in the experiments and DSC/TGA analysis. The NH_4^+ and ClO_4^- ions are going to be able to move freely,[1] and the surface−molecule distances are going to change accordingly. The variation within the N−H bonds in the lowest energy configuration for each 2D nanomaterial was at most 10% (AP on Gr). The variation within the Cl−O bonds in the lowest energy configuration for each 2D nanomaterial was at most 6% (AP on Gr). The 1O down above bottom right C configuration on Gr had a H_{AP}−$C_{graphene}$ distance of 2.38 Å, which is shorter than the initial 3 Å distance before geometry optimization. This decrease in distance between the AP and the surface suggests increased interactions between the surface and the adsorbate. The AP on the hBN

https://doi.org/10.1021/acsami.3c04021
ACS Appl. Mater. Interfaces 2023, 15, 26799−26811

surface had a smaller distance with a $H_{AP}-N_{hBN}$ distance of 2.17 Å. The closest distance between the AP and the MoS_2 surface was the $H_{AP}-S_{MoS2}$ distance of 2.42 Å. These AP-surface distances follow the same trend as the interaction energy for the Gr and the hBN surfaces, but the MoS_2 surface is an outlier.

While the closest distance between the AP and the surface does not exactly follow the trend of the interaction energies, there may be additional factors at play contributing to the total interaction energy. The AP in the lowest energy configurations on each surface has a similar orientation relative to the surface, one H atom of the ammonium is closest to the surface, and 3 oxygen atoms of the perchlorate closest to the surface are all approximately in the same plane, which suggests that more than just the closest hydrogen may be available to interact with the surface, even if they are weaker interactions at larger distances. By looking at the surfaces alone, the Gr and hBN surfaces should have the same amount of charge density available in the same surface area to interact with the AP because they are isoelectronic, whereas MoS_2 has a larger charge density because of the atoms that comprise this surface naturally have more electrons. The extra charge density may lead to stronger interactions with any adsorbates even at slightly longer distances (2.42 Å for MoS_2 vs 2.17 Å for hBN) compared to surfaces with smaller charge density at slightly smaller distances.

The amount of charge or electrons transferred between the surface and the AP can give insight into the systems at hand. Charge transfer can be determined by separately summing the Bader charges of the atoms in the surface and those in the AP adsorbate. The Bader charges for the total system, surface, AP, and components of AP can be found in Table 2. There is

Table 2. Bader Charges Calculated from DFT-Optimized Geometries (PBE-D3BJ/PW) for the Ground State, Minimum Energy Configurations of AP on Different 2D Nanomaterial Surfaces[a]

	Bader charges (|e|)					
surface	total	surface	AP	NH_4^+	ClO_4^-	interaction energy (eV)
Gr	0.124	0.15	−0.03	0.82	−0.85	−0.53
hBN	0.004	0.05	−0.05	0.84	−0.89	−0.68
MoS_2	−0.003	0.05	−0.05	0.82	−0.87	−2.85

[a]The values are presented as the sums of the Bader charges of the individual atoms in each component. Negative values show that the component has more electrons than expected from the number of valence electrons at the start of the DFT calculation. The interaction energy was calculated as the energy of the interacting system minus the energies of the individual components. Negative values mean that the interacting system was more energetically favored.

electron transfer from the surface to the AP and specifically to the anionic perchlorate portion of AP. The minimum energy configuration of AP on Gr had the smallest amount of electron transfer at around 0.03 |e| (where |e| is only the magnitude of the charge of an electron). The minimum energy configurations of AP on hBN and MoS_2 had similar values around 0.05 |e|, but the amount of electron transfer from MoS_2 to AP was slightly larger than from hBN to AP. The DFT calculations did not show any proton transfer in the minimum energy configurations of AP on these 2D nanomaterials surfaces, but they do show hydrogen bonding within the AP. This hydrogen bonding may be a first step in the proton transfer processes required in the decomposition of AP, which may occur at the elevated temperatures seen in the DSC/TGA experiments.

These computational results confirm that the AP on the MoS_2 system has the strongest interactions and AP on Gr and hBN had the weakest interactions, consistent with the experimental results. The Bader charges show that there is electron transfer from each of the surfaces to the perchlorate anionic portion of AP. Further calculations looking into the interactions of AP on a MoS_2 surface with sulfur vacancies and AP with potential transition metal catalysts can be performed to determine their effects on the interaction energies and electron transfer, compared to the baseline of AP interacting with the MoS_2 surface presented here.

CONCLUSIONS

This study demonstrated the effects of the wrapping agent on the decomposition behavior of encapsulated AP composite materials as well as improved knowledge of AP decomposition in low-pressure environments. MoS_2−EC−AP showed enhanced reactivity despite its semiconducting nature, which implied that MoS_2 forms an active transition metal catalyst during the initial stages of decomposition or promotes catalysis via defect sites (sulfur vacancies). At the chemical level, MoS_2 promoted oxidation−reduction of AP or the initial product gases, which indicates an enhanced electron transfer process. DFT calculations confirmed stronger, catalytic-like interactions and increased electron transfer for AP on MoS_2 compared to the hBN and Gr surfaces. The LTD event of MoS_2−EC−AP was most similar to a diffusion-based model (D2 or D4), indicating that the enhanced reaction becomes limited by the transfer of reactants between the solid interfaces or the removal of products. Collectively, this work demonstrates the roles of the dispersion agent and 2D nanomaterial for tuning AP reactivity while providing additional insights into the physical models governing AP decomposition.

ASSOCIATED CONTENT

Supporting Information

The Supporting Information is available free of charge at https://pubs.acs.org/doi/10.1021/acsami.3c04021.

Images of the initial orientations of the 2D nanomaterial surfaces relative to AP used for the DFT model and images of the optimized 2D nanomaterial surfaces used for the DFT model; SEM and PXRD of ammonium perchlorate coated with hBN, Gr, and MoS_2; TGA analysis and TGA of ethyl cellulose and MoS_2−EC in nitrogen and air and X-ray photoelectron spectroscopy of the MoS_2−EC nanomaterial used in this study; GC-MS data for the m/z 36 for nanocomposites; Table of TGA results and TGA curves; the first derivative of nanocomposites; and Tables summarizing TGA Kinetics and Linear fits for nanocomposites from Table of calculated energies and Bader charges (PDF)

AUTHOR INFORMATION

Corresponding Author

Alfred J. Baca − *Research Office, Chemistry Branch, US NAVY, NAWCWD, China Lake, California 93555, United States;* orcid.org/0000-0003-2193-5860; Email: alfred.j.baca2.civ@us.navy.mil

https://doi.org/10.1021/acsami.3c04021
ACS Appl. Mater. Interfaces 2023, 15, 26799−26811

Authors

Michael D. Garrison − *Research Office, Chemistry Branch, US NAVY, NAWCWD, China Lake, California 93555, United States*

Lidia Kuo − *Department of Materials Science and Engineering, Northwestern University, Evanston, Illinois 60208, United States;* orcid.org/0000-0001-8603-3660

Feiyu Xu − *Department of Chemical and Environmental Engineering, University of California, Riverside, California 92521, United States;* orcid.org/0000-0003-0671-3485

Lawrence C. Baldwin − *Research Office, Chemistry Branch, US NAVY, NAWCWD, China Lake, California 93555, United States;* orcid.org/0000-0002-2311-5690

Alexander S. Hyla − *RDT&E Department, Materials Science Branch, US NAVY, NSWC IHD, Indian Head, Maryland 20640, United States;* orcid.org/0000-0002-9451-8999

Michael R. Zachariah − *Department of Chemical and Environmental Engineering, University of California, Riverside, California 92521, United States;* orcid.org/0000-0002-4115-3324

Mark C. Hersam − *Department of Materials Science and Engineering, Northwestern University, Evanston, Illinois 60208, United States;* orcid.org/0000-0003-4120-1426

Complete contact information is available at: https://pubs.acs.org/10.1021/acsami.3c04021

Author Contributions

[⊥]A.J.B. and M.D.G. contributed equally to this work.

Funding

A.J.B. and A.S.H. would like to thank the in-house laboratory independent research (ILIR) program for funding support. The authors would also like to thank the Office of Naval Research for funding under contract number N0001420WX02135. L.K. and M.C.H. acknowledge the U.S. Department of Commerce, the National Institute of Standards and Technology (Award 70NANB19H005) as part of the Center for Hierarchical Materials Design (CHiMaD) for funding the preparation of the Gr−EC, hBN−EC, and MoS_2−EC samples.

Notes

The authors declare no competing financial interest.

■ ACKNOWLEDGMENTS

The authors would like to thank Kyle Hayes for SEM of the coated AP composite materials and Janan Hui for additional TGA experiments on MoS_2−EC−AP. A.S.H. would like to thank the Department of Defense (DoD) High Performance Computing Modernization Program (HPCMP) for computational resources.

■ REFERENCES

(1) Boldyrev, V. V. Thermal Decomposition of Ammonium Perchlorate. *Thermochim. Acta* **2006**, *443*, 1−36.

(2) Jacobs, P. W. M.; Whitehead, H. M. Decomposition and Combustion of Ammonium Perchlorate. *Chem. Rev.* **1969**, *69*, 551−590.

(3) Chaturvedi, S.; Dave, P. N. Solid Propellants: AP/HTPB Composite Propellants. *Arabian Journal of Chemistry* **2019**, *12*, 2061−2068.

(4) Aziz, A.; Mamat, R.; Ali, W. K. W.; Perang, M. R. M. Review on Typical Ingredients for Ammonium Perchlorate Based Solid Propellant. *ARPN J. Eng. Appl. Sci.* **2015**, *773*−*774*, 6188−6191.

(5) Sutton, G. P.; Biblarz, O. *Rocket Propulsion Elements*, 7th ed.; Wiley Interscience, 2000.

(6) Kraeutle, K. J. The Thermal Decomposition of Orthorhombic Ammonium Perchlorate Single Crystals. *J. Phys. Chem. A* **1970**, *74*, 1350−1356.

(7) Vyazovkin, S.; Wight, C. A. Kinetics of Thermal Decomposition of Cubic Ammonium Perchlorate. *Chem. Mater.* **1999**, *11*, 3386−3393.

(8) Tolmachoff, E. D.; Baldwin, L. C.; Essel, J. T.; Hedman, T. D.; Kalman, S. E.; Kalman, J. Effects of Select Metal Oxides on the Onset, Rate and Extent of Low Temperature Ammonium Perchlorate Decomposition. *J. Energ. Mater.* **2021**, 429−444.

(9) Kalman, J.; Hedman, T.; Varghese, B.; Dagliyan, G. Nano-Computed Tomographic Measurements of Partially Decomposed Ammonium Perchlorate Particles. *Propellants, Explos., Pyrotech.* **2017**, *42*, 1111−1116.

(10) Vargeese, A. A. Pressure Effects on Thermal Decomposition Reactions: A Thermo-Kinetic Investigation. *RSC Adv.* **2015**, *5*, 78598−78605.

(11) Bircumshaw, L. L.; Newman, B. H. The Thermal Decomposition of Ammonium Perchlorate − I. Introduction, Experimental, Analysis of Gaseous Products, and Thermal Decomposition Experiments. *Proc. R. Soc. Lond. A* **1954**, *227*, 115−132.

(12) Galwey, A. K.; Jacobs, P. W. M. High-Temperature Thermal Decomposition of Ammonium Perchlorate. *J. Chem. Soc.* **1959**, 837−844.

(13) Chang, F.-M.; Huang, C.-C.; Yeh, T.-F.; Liu, C.-S.; Leu, A.-L. Characteristics of Porous Ammonium Perchlorate and Propellants Containing Same. *Propellants, Explos., Pyrotech.* **1990**, *15*, 261−265.

(14) Hedman, T. D.; Gross, M. L. On the Thermal Stability of Partially Decomposed Ammonium Perchlorate. *Propellants, Explos., Pyrotech.* **2016**, *41*, 254−259.

(15) Jacobs, P. W. M.; Russel-Jones, A. On the Mechanism of the Decomposition of Ammonium Perchlorate. *AIAA J.* **1967**, *5*, 829−830.

(16) Stone, R. L. Differential Thermal Analysis by the Dynamic Gas Technique. *Anal. Chem.* **1960**, *32*, 1582−1588.

(17) Zhu, Y.-L.; Huang, H.; Ren, H.; Jiao, Q.-J. Kinetics of Thermal Decomposition of Ammonium Perchlorate by TG/DSC-MS-FTIR. *J. Energ. Mater.* **2014**, *32*, 16−26.

(18) Raevsky, A. V.; Manelis, G. B. On the Mechanism of Decomposition of Ammonium Perchlorate. *Dokl. AN SSSR* **1963**, *151*, 886−889.

(19) Heath, G. A.; Majer, I. R. Mass-Spectrometric Study of Thermal Decomposition of Ammonium Perchlorate. *Trans. Faraday Soc.* **1964**, *60*, 1783−1791.

(20) Zhao, X.; Li, Z.; Zhang, J.; Gong, F.; Huang, B.; Zhang, Q.; Yan, Q.-L.; Yang, Z. Regulating Safety and Energy Release of Energetic Materials by Manipulation of Molybdenum Disulfide Phase. *Chem. Eng. J.* **2021**, *411*, 128603−128609.

(21) Mani, G.; Jos, J.; Nair, P. R.; Mathew, S. Investigation of Kinetic Parameters for Ammonium Perchlorate Thermal Decomposition in Presence of gCN/CuO by TG-MS Analysis and Kinetic Compensation Correction. *J. Solid State Chem.* **2021**, *301*, 122301−122312.

(22) Cheng, J.; Zhang, R.; Liu, Z.; Li, L.; Zhao, F.; Xu, S. Thermal Decomposition Mechanism of Co-ANPYO/CNTs Nanocomposites and Their Application to the Thermal Decomposition of Ammonium Perchlorate. *RSC Adv.* **2015**, *5*, 50278−50288.

(23) Abdelhafiz, M.; Yehia, M.; Mostafa, H. E.; Wafy, T. Z. Catalytic Action of Carbon Nanotubes on Ammonium Perchlorate Thermal Behavior. *React. Kinet., Mech. Catal.* **2020**, *131*, 353−366.

(24) Paulose, S.; Raghavan, R.; George, B. K. Graphite Oxide-Iron Oxide Nanocomposites as a New Class of Catalyst for the Thermal Decomposition of Ammonium Perchlorate. *RSC Adv.* **2016**, *6*, 45977−45985.

(25) An, T.; He, W.; Chen, S.-W.; Zuo, B.-L.; Qi, X.-F.; Zhao, F.-Q.; Luo, Y.; Yan, Q.-L. Thermal Behavior and Thermolysis Mechanisms of Ammonium Perchlorate Under the Effects of Graphene Oxide-

Doped Complexes of Triaminoguanidine. *J. Phys. Chem. C* **2018**, *122*, 26956−26964.
(26) Kumar, H.; Tengli, P. N.; Mishra, V. K.; Tripathi, P.; Bhushan, A.; Mishra, P. K. The Effect of Reduced Graphene Oxide on the Catalytic Activity of Cu-Cr-O-TiO_2 to Enhance the Thermal Decomposition Rate of Ammonium Perchlorate: An Efficient Fuel Oxidizer for Solid Rocket Motors and Missiles. *RSC Adv.* **2017**, *7*, 36594−36604.
(27) Li, N.; Geng, Z.; Cao, M.; Ren, L.; Zhao, X.; Liu, B.; Tian, Y.; Hu, C. Well-Dispersed Ultrafine Mn_3O_4 Nanoparticles on Graphene as a Promising Catalyst for the Thermal Decomposition of Ammonium Perchlorate. *Carbon* **2013**, *54*, 124−132.
(28) Garrison, M. D.; Wallace, S. G.; Baldwin, L. C.; Guo, Z.; Kuo, L.; Estevez, J. E.; Briseno, A. L.; Hersam, M. C.; Baca, A. J. Accelerated Decomposition Kinetics of Ammonium Perchlorate via Conformal Graphene Coating. *Chem. Mater.* **2021**, *33*, 9608−9617.
(29) Grossman, K. D.; Sakthivel, T. S.; Dillier, C.; Petersen, E. L.; Seal, S. Effect of Amine-Modified Boron Nitride (BN) on Ammonium Perchlorate Decomposition. *RSC Adv.* **2016**, *6*, 89635−89641.
(30) de Moraes, A. C. M.; Hyun, W. J.; Seo, J.-W. T.; Downing, J. R.; Lim, J.-M.; Hersam, M. C. Ion-Conductive, Viscosity-Tunable Hexagonal Boron Nitride Nanosheet Inks. *Adv. Funct. Mater.* **2019**, *29*, No. 1902245.
(31) de Moraes, A. C. M.; Obrzut, J.; Sangwan, V. K.; Downing, J. R.; Chaney, L. E.; Patel, D. K.; Elmquist, R. E.; Hersam, M. C. Elucidating Charge Transport Mechanisms in Cellulose-Stabilized Graphene Inks. *J. Mater. Chem. C* **2020**, *8*, 15086−15091.
(32) Hassel, O.; Mark, H. Über die Kristallstruktur des Graphits. *Zeitschrift für Physik* **1924**, *25*, 317−337.
(33) Kurakevych, O. O.; Solozhenko, V. L. Rhombohedral Boron Subnitride, $B_{13}N_2$, by X-ray Powder Diffraction. *Acta Crystallogr., Sect. C: Struct. Chem.* **2007**, *63*, i80−i82.
(34) Murray, R.; Evans, B. The Thermal Expansion of 2*H*-MoS_2 and 2*H*-WSe_2 Between 10 and 320 K. *J. Appl. Cryst.* **1979**, *12*, 312−315.
(35) Giannozzi, P.; Baroni, S.; Bonini, N.; Calandra, M.; Car, R.; Cavazzoni, C.; Ceresoli, D.; Chiarotti, G. L.; Cococcioni, M.; Dabo, I.; Dal Corso, A.; Fabris, S.; Fratesi, G.; de Gironcoli, S.; Gebauer, R.; Gerstmann, U.; Gougoussis, C.; Kokalj, A.; Lazzeri, M.; Martin-Samos, L.; Marzari, N.; Mauri, F.; Mazzarello, R.; Paolini, S.; Pasquarello, A.; Paulatto, L.; Sbraccia, C.; Scandolo, S.; Sclauzero, G.; Seitsonen, A. P.; Smogunov, A.; Umari, P.; Wentzcovitch, R. M. QUANTUM ESPRESSO: A Modular and Open-Source Project for Quantum Simulations of Materials. *J. Phys.: Condens. Matter* **2009**, *21*, No. 395502.
(36) Giannozzi, P.; Andreussi, O.; Brumme, T.; Bunau, O.; Buongiorno Nardelli, M.; Calandra, M.; Car, R.; Cavazzoni, C.; Ceresoli, D.; Cococcioni, M.; Colonna, N.; Carnimeo, I.; Dal Corso, A.; de Gironcoli, S.; Delugas, P.; DiStasio Jr, R. A.; Ferretti, A.; Floris, A.; Fratesi, G.; Fugallo, G.; Gebauer, R.; Gerstmann, U.; Giustino, F.; Gorni, T.; Jia, J.; Kawamura, M.; Ko, H.-Y.; Kokalj, A.; Küçükbenli, E.; Lazzeri, M.; Marsili, M.; Marzari, N.; Mauri, F.; Nguyen, N. L.; Nguyen, H.-V.; Otero-de-la-Roza, A.; Paulatto, L.; Poncé, S.; Rocca, D.; Sabatini, R.; Santra, B.; Schlipf, M.; Seitsonen, A. P.; Smogunov, A.; Timrov, I.; Thonhauser, T.; Umari, P.; Vast, N.; Wu, X.; Baroni, S. Advanced Capabilities for Materials Modelling with Quantum ESPRESSO. *J. Phys.: Condens. Matter* **2017**, *29*, No. 465901.
(37) Blöchl, P. E. Projector Augmented-Wave Method. *Phys. Rev. B: Condens. Matter Mater. Phys.* **1994**, *50*, 17953−17979.
(38) Perdew, J. P.; Burke, K.; Ernzerhof, M. Generalized Gradient Approximation Made Simple. *Phys. Rev. Lett.* **1996**, *77*, 3865−3868.
(39) Perdew, J. P.; Burke, K.; Ernzerhof, M. Generalized Gradient Approximation Made Simple [Phys. Rev. Lett. 77, 3865 (1996)] Errata. *Phys. Rev. Lett.* **1997**, *78*, 1396.
(40) Grimme, S.; Ehrlich, S.; Goerigk, L. Effect of the Damping Function in Dispersion Corrected Density Functional Theory. *J. Comput. Chem.* **2011**, *32*, 1456−1465.
(41) Tang, W.; Sanville, E.; Henkelman, G. A Grid-Based Bader Analysis Algorithm Without Lattice Bias. *J. Phys.: Condens. Matter* **2009**, *21*, No. 084204.
(42) Jacquemin, D.; Bahers, T. L.; Adamo, C.; Ciofini, I. What Is the 'Best' Atomic Charge Model to Describe Through-Space Charge-Transfer Excitations? *Phys. Chem. Chem. Phys.* **2012**, *14*, 5383−5388.
(43) Marzari, N. Ab-initio Molecular Dynamics for Metallic Systems. Ph.D. Dissertation, University of Cambridge: Cambridge, UK, 1996.
(44) Press, W. H.; Teukolsky, S. A.; Vetterling, W. T.; Flannery, B. P. *Numerical Recipes: The Art of Scientific Computing*, 3rd ed.; Cambridge University Press: Cambridge, UK, 2007.
(45) Frisch, M. J.; Trucks, G. W.; Schlegel, H. B.; Scuseria, G. E.; Robb, M. A.; Cheeseman, J. R.; Scalmani, G.; Barone, V.; Petersson, G. A.; Nakatsuji, H.; Li, X.; Caricato, M.; Marenich, A. V.; Bloino, J.; Janesko, B. G.; Gomperts, R.; Mennucci, B.; Hratchian, H. P.; Ortiz, J. V.; Izmaylov, A. F.; Sonnenberg, J. L.; Williams-Young, D.; Ding, F.; Lipparini, F.; Egidi, F.; Goings, J.; Peng, B.; Petrone, A.; Henderson, T.; Ranasinghe, D.; Zakrzewski, V. G.; Gao, J.; Rega, N.; Zheng, G.; Liang, W.; Hada, M.; Ehara, M.; Toyota, K.; Fukuda, R.; Hasegawa, J.; Ishida, M.; Nakajima, T.; Honda, Y.; Kitao, O.; Nakai, H.; Vreven, T.; Throssell, K.; Montgomery, J. A., Jr.; Peralta, J. E.; Ogliaro, F.; Bearpark, M. J.; Heyd, J. J.; Brothers, E. N.; Kudin, K. N.; Staroverov, V. N.; Keith, T. A.; Kobayashi, R.; Normand, J.; Raghavachari, K.; Rendell, A. P.; Burant, J. C.; Iyengar, S. S.; Tomasi, J.; Cossi, M.; Millam, J. M.; Klene, M.; Adamo, C.; Cammi, R.; Ochterski, J. W.; Martin, R. L.; Morokuma, K.; Farkas, O.; Foresman, J. B.; Fox, D. J. *Gaussian 16*; revision C.01; Gaussian, Inc.: Wallingford CT, USA, 2016.
(46) Kohga, M.; Tsuzuki, H. Crystal Habit Modification of Ammonium Perchlorate by Ethylene Glycol. *Adv. Powder Technol.* **2010**, *21*, 443−447.
(47) Secor, E. B.; Gao, T. Z.; Islam, A. E.; Rao, R.; Wallace, S. G.; Zhu, J.; Putz, K. W.; Maruyama, B.; Hersam, M. C. Enhanced Conductivity, Adhesion, and Environmental Stability of Printed Graphene Inks with Nitrocellulose. *Chem. Mater.* **2017**, *29*, 2332−2340.
(48) Halawy, S. A.; Mohamed, M. A. The Role of MoO_3 and Fe_2O_3 in the Thermal Decomposition of Ammonium Perchlorate. *Collect. Czech. Chem. Commun.* **1994**, *59*, 2253−2261.
(49) Mitchell, P. C. H.; Outteridge, T.; Kloska, K.; McMahon, S.; Epshteyn, Y.; Sebenik, R. F.; Burkin, A. R.; Dorfler, R. R.; Laferty, J. M.; Leichtfried, G.; Meyer-Grünow, H.; Vukasovich, M. S. Molybdenum and Molybdenum Compounds. *Ullmann's Encyclopedia of Industrial Chemistry* **2022**.
(50) Ye, G.; Gong, Y.; Lin, J.; Li, B.; He, Y.; Pantelides, S. T.; Zhou, W.; Vajtai, R.; Ajayan, P. M. Defects Engineered Monolayer MoS_2 for Improved Hydrogen Evolution Reaction. *Nano Lett.* **2016**, *16*, 1097−1103.
(51) Gao, X.; Bian, G.; Zhu, J. Electronics from Solution-Processed 2D Semiconductors. *J. Mater. Chem. C* **2019**, *7*, 12835−12861.
(52) Friedman, H. L. Kinetics of Thermal Degradation of Char-Forming Plastics from Thermogravimetry. Application to a Phenolic Plastic. *J. Polym. Sci., Part C: Polym. Symp.* **2007**, *6*, 183−195.
(53) Venkatesh, M.; Ravi, P.; Tewari, S. P. Isoconversional Kinetic Analysis of Decomposition of Nitroimidazoles: Friedman Method vs Flynn-Wall-Ozawa Method. *J. Phys. Chem. A* **2013**, *117*, 10162−10169.
(54) Barrie, P. J. The Mathematical Origins of the Kinetic Compensation Effect: 1. The Effect of Random Experimental Errors. *Phys. Chem. Chem. Phys.* **2012**, *14*, 318−326.
(55) Barrie, P. J. The Mathematical Origins of the Kinetic Compensation Effect: 2. The Effect of Systematic Experimental Errors. *Phys. Chem. Chem. Phys.* **2012**, *14*, 327−336.
(56) Sánchez-Jiménez, P. E.; Pérez-Maqueda, L. A.; Perejón, A.; Criado, J. M. Generalized Kinetic Master Plots for the Thermal Degradation of Polymers Following a Random Scission Mechanism. *J. Phys. Chem. A* **2010**, *114*, 7868−7876.
(57) Khawam, A.; Flanagan, D. R. Solid-State Kinetic Models: Basics and Mathematical Fundamentals. *J. Phys. Chem. B* **2006**, *110*, 17315−17328.

https://doi.org/10.1021/acsami.3c04021
ACS Appl. Mater. Interfaces 2023, 15, 26799−26811